



## RESEARCH ARTICLE

10.1029/2020JD034137

# Diversity of the Boreal Summer Intraseasonal Oscillation

Guosen Chen<sup>1</sup>  and Bin Wang<sup>1,2</sup> 

### Key Points:

- Three types of boreal summer intraseasonal oscillation (BSISO) have been identified, which exhibit various 2D propagation features
- The diverse propagation features are attributed to the BSISO circulation structural differences
- The variations in the season-dependent background can cause differences in the BSISO circulation structures

### Correspondence to:

G. Chen,  
guosen@nuist.edu.cn

### Citation:

Chen, G., & Wang, B. (2021). Diversity of the boreal summer intraseasonal oscillation. *Journal of Geophysical Research: Atmospheres*, 126, e2020JD034137. <https://doi.org/10.1029/2020JD034137>

Received 23 OCT 2020

Accepted 5 APR 2021

<sup>1</sup>Earth System Modeling Center, Key Laboratory of Meteorological Disaster of Ministry of Education, Collaborative Innovation Center on Forecast and Evaluation of Meteorological Disasters, Nanjing University of Information Science and Technology, Nanjing, China, <sup>2</sup>Department of Atmospheric Sciences and International Pacific Research Center, The University of Hawaii at Manoa, Honolulu, HI, USA

**Abstract** Boreal summer intraseasonal oscillation (BSISO) profoundly impacts Northern Hemisphere monsoon onsets and breaks, tropical cyclones, and many climate extremes. BSISO exhibits more complex propagation patterns than the dominant eastward propagation of the Madden-Julian Oscillation. Previous studies have extensively examined the dominant northeastward propagating BSISO mode and its northward component, but this mode only accounts for about half of the total cases. We conducted an objective cluster analysis of the two-dimensional BSISO propagation and revealed two new forms of BSISO propagation besides the northeastward propagation: the dipolar northward propagation and the eastward expansion. We investigate processes governing the different propagation forms using moisture tendency analysis. We show that the propagation diversity is related to BSISO's circulation structural asymmetries and the associated moistening processes. The Rossby-wave component in the background zonal wind shear favors northward propagation while the Kelvin-wave component favors eastward propagation. The circulation differences are affected by the variation of background states, especially those season-dependent variations. The results provide insights into the BSISO diversity and potential precursors for foreseeing BSISO propagation.

## 1. Introduction

Tropical intraseasonal oscillation (ISO) exhibits pronounced seasonality (Madden, 1986; B. Wang & Rui, 1990). The boreal summer intraseasonal oscillation (BSISO), active mainly over the Indo-Pacific warm pool region, is more complicated than its winter counterpart, the Madden-Julian Oscillation (MJO) (Madden & Julian, 1971, 1972), due to the coexistence of equatorial eastward, off-equatorial westward, and northward propagating low-frequency modes and their interactions (Lau & Chan, 1986; Pillai & Sahai, 2016; B. Wang & Xie, 1997).

The BSISO has profound impacts on global weather and climate systems (Krishnamurti & Subrahmanyam, 1982; Zhang, 2013), such as monsoon onsets and breaks (T. C. Chen et al., 2000; B. Goswami, 2012; B. N. Goswami & Xavier, 2003; Krishnamurthy & Shukla, 2000; Sikka & Gadgil, 1980), tropical cyclones (B. N. Goswami et al., 2003; Moon et al., 2018; Nakazawa, 1986), floods and droughts (Parthasarathy & Mooley, 1978; Yihui et al., 2004), extreme surface temperature (Naumann & Vargas, 2010), and many more. Successful prediction of BSISO is of great social and economic concern, but it remains a significant challenge (S.-S. Lee et al., 2015; J. Neena et al., 2017; J. M. Neena et al., 2014). One of the problems is that the numerical model cannot realistically simulate the propagation features of the BSISO, such as the northward propagation over the Asian monsoonal regions (Jiang et al., 2018; J. Neena et al., 2017).

Besides eastward propagation from the Indian Ocean (IO) to western Pacific (WP), BSISO exhibits salient northward propagation over the Asian-Pacific monsoon region and off-equatorial westward propagation over the northern WP (T. C. Chen & Murakami, 1988; Kemball-Cook & Wang, 2001; Krishnamurti & Subrahmanyam, 1982; Lau & Chan, 1986; Murakami et al., 1984; B. Wang & Rui, 1990; Yasunari, 1979, 1980). Statistically, the canonical BSISO, defined as the leading modes of multivariate empirical orthogonal function (EOF) analysis on outgoing longwave radiation (OLR) and low-level wind anomalies (Kikuchi et al., 2012; J.-Y. Lee et al., 2013; Wheeler & Hendon, 2004), usually originate from the equatorial IO and propagates eastward and northward simultaneously, forming a northwest-southeast tilted convection band due to stretching by the eastward and northward propagation and finally decaying over the South China Sea (SCS). However, there is a considerable deviation from this canonical form, manifested by the diverse phase

© 2021. The Authors.

This is an open access article under the terms of the [Creative Commons Attribution-NonCommercial License](https://creativecommons.org/licenses/by-nc/4.0/), which permits use, distribution and reproduction in any medium, provided the original work is properly cited and is not used for commercial purposes.

evolution of individual events (J.-Y. Lee et al., 2013). It was shown that the canonical northeastward propagating BSISO accounts for about only half of the BSISO events (Pillai & Sahai, 2016; B. Wang & Rui, 1990) that have origins over the IO. Besides the canonical propagation form, it was also found that there are independent northward propagating BSISO (Pillai & Sahai, 2016; B. Wang & Rui, 1990). The propagation tracks of BSISO also show sub-seasonal dependence (Kemball-Cook & Wang, 2001). Comprehensive knowledge of the causes of diverse BSISO propagation tracks is critical for understanding BSISO propagation mechanisms and improving model simulation and prediction of BSISO.

A pilot study of MJO diversity was focused on northern winter MJO (B. Wang et al., 2019). The MJO diversity was studied by cluster analysis on one-dimensional equatorial eastward propagation of the MJO. However, the study of the BSISO diversity requires an analysis of two-dimensional (2D) movement of the BSISO convective activity. Such an objective and systematic study has not yet emerged. Previous studies on BSISO diversity are either subjective (e.g., B. Wang & Rui, 1990) or not systematic (e.g., Pillai & Sahai, 2016, in that study the propagation directions are pre-defined). This work attempts a systematic and objective description of BSISO propagation diversity and an in-depth grasp of underlying mechanisms.

The frequency of BSISO has two spectrum peaks. One is on a 30–80 day period, and the other is on a 10–30 day period (J.-Y. Lee et al., 2013). In this study, we focus on the 30–80 day regime. Moreover, we focus on those BSISO events that originate from IO, as IO is a primary origin for BSISO events (Lau & Chan, 1986; B. Wang & Rui, 1990). We will reveal the diversity of 2D propagation forms associated with the observed BSISO using an objective and systematic method, and explore the causes of propagation diversity to seek potential precursors for predicting the BSISO propagation. The results may advance our understanding of the mechanisms governing the complex BSISO propagation behaviors and improve the BSISO simulation and prediction.

## 2. Materials and Methods

### 2.1. Data and Method

The daily averaged OLR data on a  $2.5^\circ$  squared resolution from NCEP/NOAA interpolated OLR data set (Liebmann & Smith, 1996) for the period of 1979–2016 (38 years) are used here to represent the convection signals over the tropics. For the horizontal and vertical winds, temperature, geopotential height, specific humidity, and sea surface temperature (SST), we use daily averaged ERA-Interim reanalysis data (Dee et al., 2011). The surface latent flux is also obtained from ERA-Interim. The reanalysis data were interpolated to  $2.5^\circ \times 2.5^\circ$  grids in order to match with the OLR data. The anomalous intraseasonal fields were obtained by first removing the time mean and climatological annual cycle, and then applying a 30–80 day band-pass filter (Duchon, 1979).

### 2.2. Cluster Analysis

Following B. Wang et al. (2019), the K-means cluster analysis is used to objectively classify the BSISO events according to their propagation patterns. The K-means method clusters data by dividing the samples into several groups of equal variances, minimizing a criterion known as within-cluster sum-of-squares (Kaufman & Rousseeuw, 2009). In short, the K-means method finds a classification of data such that objects within each cluster are as close to each other as possible, and as far from objects in other clusters as possible.

To apply K-means method to cluster BSISO events, the first step is to identify individual BSISO event. Since the equatorial IO is a popular origin for the BSISO events (Lau & Chan, 1986; B. Wang & Rui, 1990), we define a BSISO event if the box-averaged intraseasonal OLR over the equatorial IO ( $5^\circ\text{S}$ – $10^\circ\text{N}$ ,  $80^\circ$ – $100^\circ\text{E}$ ) is below its mean minus one standard deviation. There are 102 events during the 38 year (1979–2016) boreal summer (May to October) period. We choose a reference date, defined as day 0, for a selected BSISO event as the day when the box-averaged OLR over equatorial IO ( $5^\circ\text{S}$ – $10^\circ\text{N}$ ,  $80^\circ$ – $100^\circ\text{E}$ ) reaches its minimum.

The second step is to apply cluster analysis to the sequential pentad mean maps of the intraseasonal OLR anomalies associated with the selected events. As the duration of a phase (out of total eight phases for a cycle) for the 30–80-day BSISO modes is about a pentad, using sequential pentad mean maps could well depict the phase evolution of the BSISO. The pentad 0 is defined as the pentad mean of intraseasonally filtered

daily data with the central date being day 0. Pentad 1 (−1) is defined as pentad mean succeeding (preceding) pentad 0, and so on. The temporal domain for cluster analysis is from pentad −1 to pentad 3, while the spatial domain is from 60°E to 170°E and 15°S to 25°N. A five-point zonal running mean smoothing is applied to the pentad maps to remove small scale noises before applying the cluster analysis.

In K-means cluster analysis, a “distance” between each object in data must be defined so that we can measure how close each cluster member is to the corresponding cluster centroid. Here, we use squared Euclidean distance as the metric of “distance.” To perform the K-means analysis, one needs to specify the number of clusters, which is determined by the silhouette values that measures how well a cluster member is clustered. The optimal cluster number is determined if an increase of cluster number leads to a sharp decrease of mean silhouette value. Based on this criterion, three clusters are optimal for the selected BSISO events. In our analysis, the cluster members with silhouette values lower than 0.05 are further excluded from the corresponding clusters as they are considered “poorly” clustered. By removing 13 “outliers,” 89 events remain in the three clusters.

The composite analysis is then applied to the three BSISO clusters to compare their structures. To remove small scale noise, a five-point zonal running mean smoothing is applied to the intraseasonally filtered data when performing the composite analysis.

### 2.3. Moisture Tendency Diagnosis

As the tropical precipitation or convection activity is tied to the column integrated moisture (Bretherton et al., 2004), we will analyze the moisture budget to diagnose the propagation mechanisms of the BSISO convection. The vertically integrated moisture equation is:

$$\frac{\partial \langle q \rangle'}{\partial t} = -\langle \mathbf{V} \cdot \nabla q \rangle' - \langle \omega \frac{\partial q}{\partial p} \rangle' - \langle Q_2 \rangle' / L \quad (1)$$

where  $q$  is the specific humidity,  $\mathbf{V}$  is the horizontal components of the wind,  $\omega$  is the vertical velocity, and  $L$  is the latent heat of vaporization. The angle brackets represent mass-weighted vertical integration from 1,000 to 200 hPa, and the primes denote the intraseasonal component.  $Q_2$  is the moisture sinks defined by Yanai et al. (1973). In tropics, the  $Q_2$  to some extent represents the condensational heating.  $\langle Q_2 \rangle' / L \approx (P - E)$  represents the column integrated moisture sinks, where  $P$  is the precipitation (condensation) and  $E$  is the evaporation. Since in the convection zone, the vertical moisture advection often collocates with the condensation and they tend to cancel each other, we define an in-column process as  $-\langle \omega \frac{\partial q}{\partial p} \rangle' - \frac{\langle Q_2 \rangle'}{L} - E' \approx -\langle \omega \frac{\partial q}{\partial p} \rangle' - P'$ , which represents the net vertical moistening due to convection and large-scale dynamics. The terms of Equation 1 are first calculated by daily data and then the filtering process described above was applied to the variable to retrieve the intraseasonal component.

To further identify the relative contribution of eddy-eddy and eddy-mean flow interactions on the horizontal moisture advection, we decompose each variable into a background low-frequency (>90 days) component, an intraseasonal component (30–80 days), and a high-frequency (<30 days) component. Thus, the horizontal moisture advection can be expressed as:

$$-\langle \mathbf{V} \cdot \nabla q \rangle' = -\langle \mathbf{V}' \cdot \nabla \bar{q} \rangle' - \langle \bar{\mathbf{V}} \cdot \nabla q' \rangle' - \langle \mathbf{V}^* \cdot \nabla q^* \rangle' + res'' \quad (2)$$

where overbar denotes background low-frequency component, asterisk denotes high frequency component, and  $res''$  denotes the residual term of the horizontal moisture advection.

## 3. Diversity of BSISO Propagation and the Associated Circulation Features

102 BSISO events during the 38 year (1979–2016) boreal summer (May to October) period are identified based on the convective anomalies over the equatorial IO (5°S–10°N, 80°–100°E). The K-means analysis clusters these BSISO events into three optimal clusters (see Materials and Methods section for details).

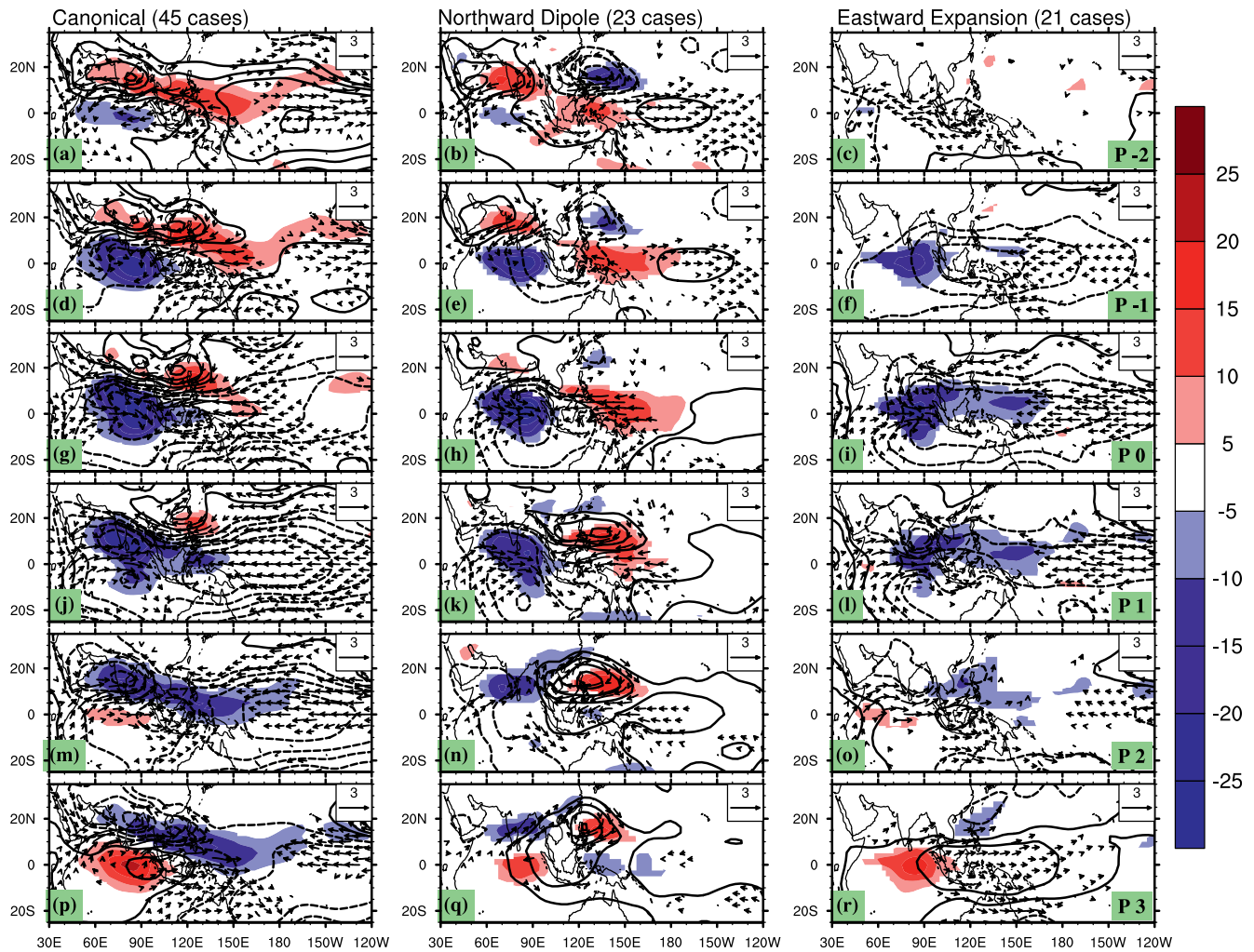


**Figure 1.** Time evolution of OLR and low-level circulation for the three BSISO modes. Shown are composited OLR anomalies (shading, in units of  $\text{W m}^{-2}$ ), 850 hPa normalized geopotential height anomalies (contour with an interval of 0.3), and anomalous winds (vector, in units of  $\text{m s}^{-1}$ ) from pentad  $-2$  to pentad  $3$  for (left column) the canonical mode, (middle column) the northward dipole mode, and (right column) the eastward expansion mode. The solid contour indicates positive value, the dashed contour indicates negative value, and the zero contour is omitted. The normalized geopotential height anomaly on each grid point is obtained through dividing the geopotential height anomaly by its corresponding standard deviation. Pentad  $0$  (denoted as  $P_0$ ) is the pentad mean with day  $0$  (when the equatorial Indian Ocean OLR reaches a minimum) being the central date, and pentad  $1$  is the pentad succeeding the pentad  $0$ . The OLR and wind vectors are only shown for those above the 95% confidence level.

Figure 1 shows that the three BSISO clusters exhibit distinct 2D propagation forms. In the first cluster (left column), the enhanced convection originates from IO (pentad  $-2$ ) and propagate northward and eastward simultaneously, stretching into a tilted convection band from India to the equatorial WP. The period of this cluster is about 40 days, implied by the out-of-phase relation between pentad  $-1$  and pentad  $3$ . This cluster essentially resembles the leading BSISO mode defined by the multivariate EOF (J.-Y. Lee et al., 2013; Wheeler & Hendon, 2004). Therefore, we refer to this cluster as canonical mode.

The second cluster (middle column) features a northward propagating east-west seesaw dipole between the IO and WP. This is manifested by the northward propagation of a dipole (with enhanced convection over IO and suppressed convection over WP) from equator (pentad  $-2$ ) to India and SCS (pentad  $3$ ). Note that as this dipole propagates northward, there is a reversed dipole developed to its south (pentad  $2$  and  $3$ ), signifying the development of second half cycle. Since the northward propagation is predominant in this cluster without eastward propagation, we refer to this cluster as northward dipole mode. The period for this cluster is about 40–50 days.



The third cluster (right column) is a relatively weak eastward propagating mode with an approximate 40 day period. Note that the enhanced convection center over central IO is primarily stationary (not propagating) from pentad  $-1$  to  $+1$  but with an intensification from pentad  $-1$  to pentad  $0$ . The eastward “propagation” in this cluster is essentially a sudden eastward expansion of convection anomalies from the IO to WP on pentad  $0$  and followed by the decay of convection over the IO and WP from pentad  $1$  to  $2$ . For this reason, we call it eastward expansion mode.

What are the circulation features associated with these BSISO modes? In tropics, the circulation associated with the low-frequency convective heating is primarily depicted by the Kelvin-wave response and the Rossby-wave response (Gill, 1980). The Kelvin-wave response to the east of enhanced convection heating in low level is manifested as low pressure and easterly wind anomalies that have Gaussian distribution about equator, while the Rossby-wave response to the west of enhanced convection heating in low level is manifested as a pair of cyclonic gyres straddling about the equator, with westerly wind anomalies over the equator and easterly wind anomalies to the north of equator.

As shown by Figure 1, a noticeable feature distinguishing the modes having eastward propagation (the canonical mode and eastward expansion mode) and the northward propagating dipole mode is the strength of the Kelvin-wave response to the east of convection. In the canonical mode and eastward expansion mode, there are prominent signals of Kelvin-wave response to the east of the enhanced IO convection (e.g., pentad  $-1$  to  $1$ ). In contrast, in the northward dipole mode the signals of Kelvin-wave response to the east of the convection anomalies are weak (pentad  $-1$  and  $0$ ) or absent (other pentads). On the other hand, the strength of the Rossby-wave zonal winds to the north of the equatorial convection anomalies distinguishes the modes having northward propagating (the canonical mode and the northward dipole mode) and the eastward expansion mode. In the canonical mode and the northward dipole mode, the Rossby-wave responses are more zonally oriented, and the associated zonal wind anomalies are significant, while in the eastward propagating mode the Rossby-wave response is more meridionally elongated (pentad  $0$  and  $1$ ), and the associated zonal wind anomalies are weak.

The finding here suggests that different propagation patterns of BSISO are associated with distinct circulation structures along the propagation directions. This view expands the previous finding that the MJO eastward propagation is associated with the zonal circulation asymmetries (B. Wang & Lee, 2017; B. Wang, Lee, et al., 2018). The findings here also support that the Kelvin-wave response is a driver for the eastward propagation of tropical ISO (G. Chen & Wang, 2018, 2019; 2020; Hendon & Salby, 1994; Maloney & Hartmann, 1998; Matthews et al., 2004; Salby et al., 1994; B. Wang et al., 2019), while the northward propagation is associated with the Rossby-wave response (DeMott et al., 2013; Hsu & Weng, 2001; K-M. Lau & Peng, 1990; Lawrence & Webster, 2002; Li, 2014; B. Wang & Xie, 1997).

## 4. Diagnosis of Moisture Tendency for Eastward and Northward Propagation

How can the circulation structural differences lead to the diverse propagation of BSISO? Since it can be shown that the convection anomalies shown in Figure 1 are well collocated with the column-integrated specific humidity anomalies, we will investigate the moisture budget to see what processes generate eastward or northward propagation tendency and how these processes are related to the circulation differences among various BSISO modes.

### 4.1. Northeastward Propagation of the Canonical Mode

Figure 2 shows the spatial patterns of the moisture budgets for the three BSISO modes on pentad  $0$ . For the northeastward propagating canonical mode, the positive moisture tendency is located to the northeast of the IO enhanced convection (Figure 2a), signifying the northeastward propagation. The horizontal moisture advection contributes to the positive tendency to the north of the IO convective center (Figure 2d), which is principally collocated with the Rossby-wave zonal wind anomalies, consistent with previous studies (Adames et al., 2016; Jiang et al., 2018). Figure 3 further quantifies each term’s relative contribution to the positive tendencies over the IO sector ( $50^{\circ}$ – $100^{\circ}$ E). It confirms that the horizontal moisture advection is the main process causing the northward propagation tendency. It can be shown that this positive horizontal moisture advection is dominated by the advection of background moisture by the intraseasonal winds

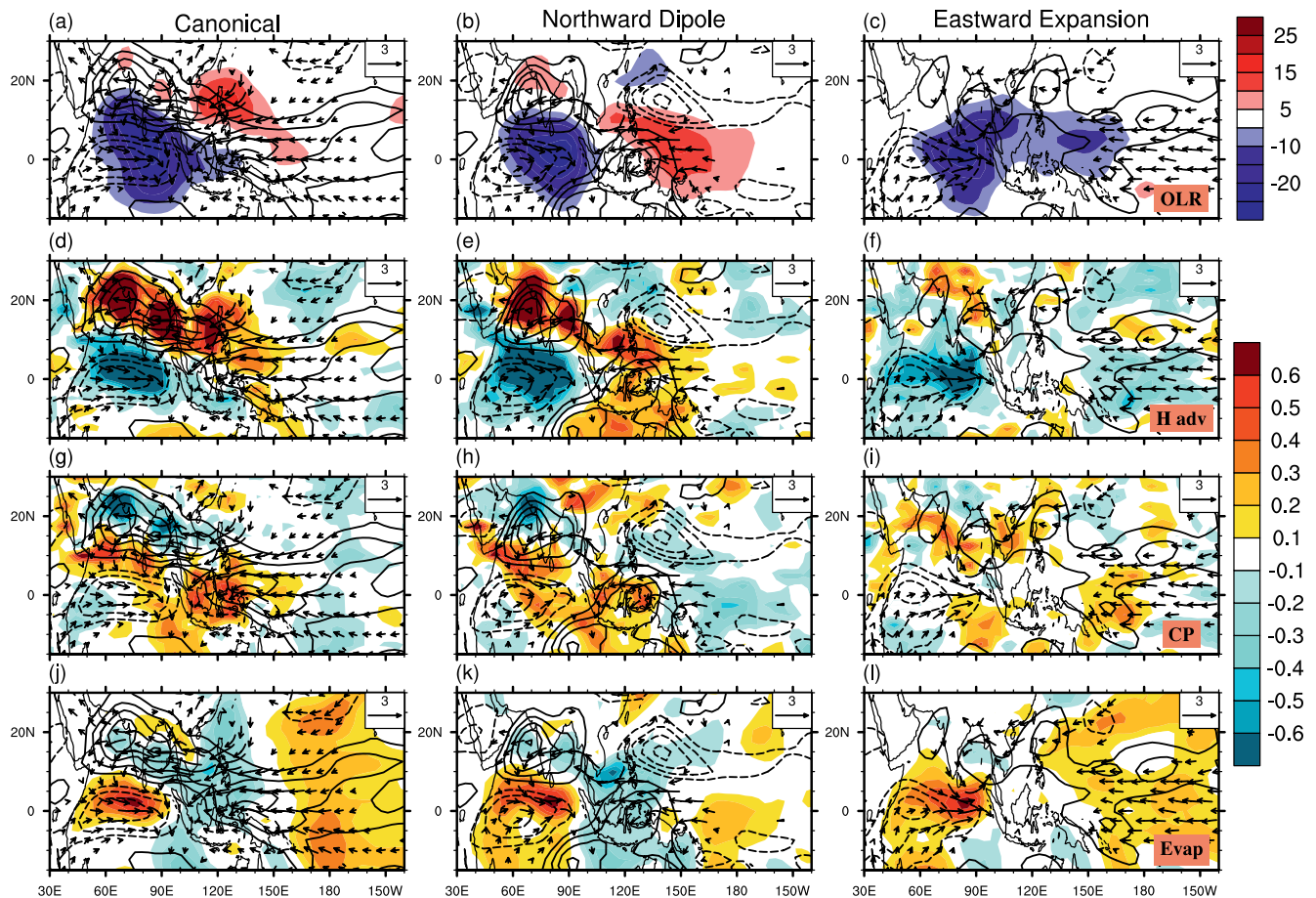


**Figure 2.** Moisture budget on pentad 0 for the three BSISO mode. The first row shows the OLR anomalies (shading, in units of  $\text{W m}^{-2}$ ), the second row shows the horizontal moisture advection (shading, in units of  $\text{kg m}^{-2} \text{ day}^{-1}$ ), the third row shows the in-column process (combined effect of moistening by vertical moisture advection and drying by precipitation, shading, in unit of  $\text{kg m}^{-2} \text{ day}^{-1}$ ), and the fourth row shows the surface evaporation (shading, in units of  $\text{kg m}^{-2} \text{ day}^{-1}$ ). Also shown in each panel are the corresponding moisture tendency (contour with an interval of  $0.1 \text{ kg m}^{-2} \text{ day}^{-1}$ ) and 850 hPa winds (vector, in units of  $\text{m s}^{-1}$ ). The solid contour indicates positive value, the dashed contour indicates negative value, and the zero contour is omitted. The wind vectors are only shown for those above the 95% confidence level.

(Figure 4a), consistent with the previous analysis (Jiang et al., 2018; Pillai & Sahai, 2016). In fact, the advection of background moisture by intraseasonal winds was found to be an important factor in triggering the monsoonal active or break conditions over India (Annamalai, 2010). The horizontal moisture advection also contributes to the positive tendency to the northeast of the IO convection center over the Southeast Asia (Figure 2d), which is attributed to the advection of intraseasonal moisture by the background monsoonal wind (see Figure 5). The advection of intraseasonal moisture anomalies by the background winds was found to be important in simulating the northward propagation of BSISO (Ajayamohan et al., 2011). The combined effect of the horizontal moisture advection (Figures 5d and 5g) forms a tilted positive moisture tendency band to the northeast of the IO active convection.

On the other hand, the positive moisture tendencies to the east of the IO enhanced convection over the equatorial Maritime continent (MC) are mainly attributed to the in-column process (Figure 2g), which leads to eastward propagation of IO enhanced convection toward the MC (Figures 1g and 1j). This contrasts with the MJO in boreal winter, of which the horizontal moisture advection is found to play a more significant role for the eastward propagation (Jiang, 2017; Jiang et al., 2020; Kim et al., 2014, 2017; Maloney, 2009).

This in-column process over MC, the net vertical moistening due the convection and large-scale dynamics, is associated with the circulation anomalies in the east-west direction. Figure 6a shows that to the east of the IO enhanced convection center, the low-level moistening coincides with the ascending motions induced by

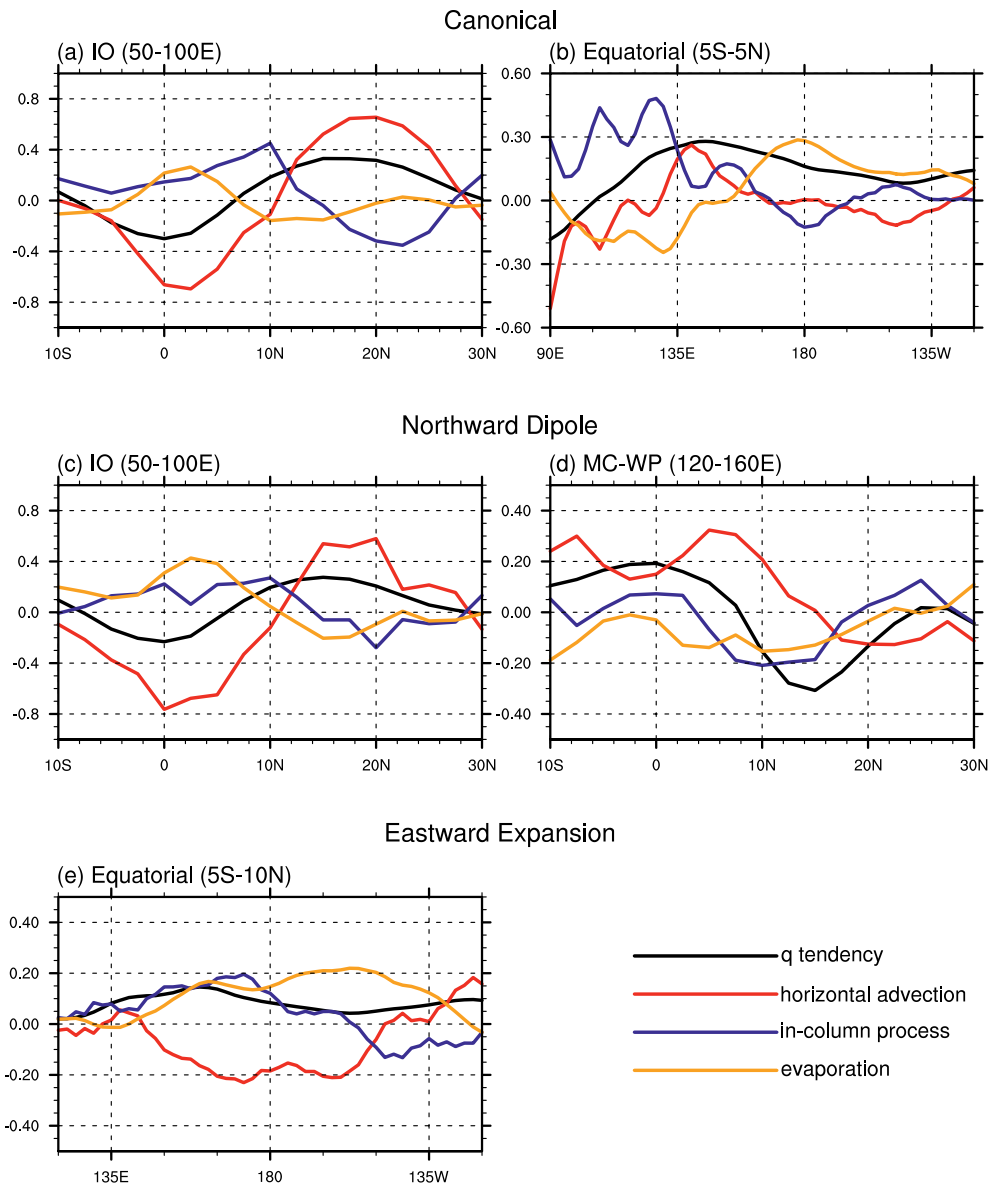


**Figure 3.** The moisture budget over different regions: (a) IO (50°–100°E averaged) and (b) equatorial IO-WP (5°S–5°N averaged) for the canonical mode; (c) IO (50°–100°E averaged) and (d) MC-WP (120°–160°E averaged) for Northward Dipole mode; (e) equatorial IO-WP (5°S–10°N averaged) for eastward expansion mode.

the boundary layer convergence, suggesting that the shallow and congestus convection induced by the Kelvin-wave-related boundary layer convergence plays an important role in generating the eastward moisture tendency (Adames, 2017; G. Chen & Wang, 2018; B. Wang et al., 2019; L. Wang & Li, 2020).

As also shown by Figures 2j and 3b, the evaporation contributes to the positive moisture tendencies over the equatorial central Pacific. These evaporation anomalies are caused by the Kelvin-wave easterly anomalies superposed on the background mean easterly flows over the equatorial central Pacific.

In short, the northward propagation of the canonical mode over IO is mainly driven by the moistening caused by horizontal moisture advection associated with the Rossby-wave response, while the eastward propagation along equator is mainly driven by the moistening caused by in-column process associated with the Kelvin-wave response.

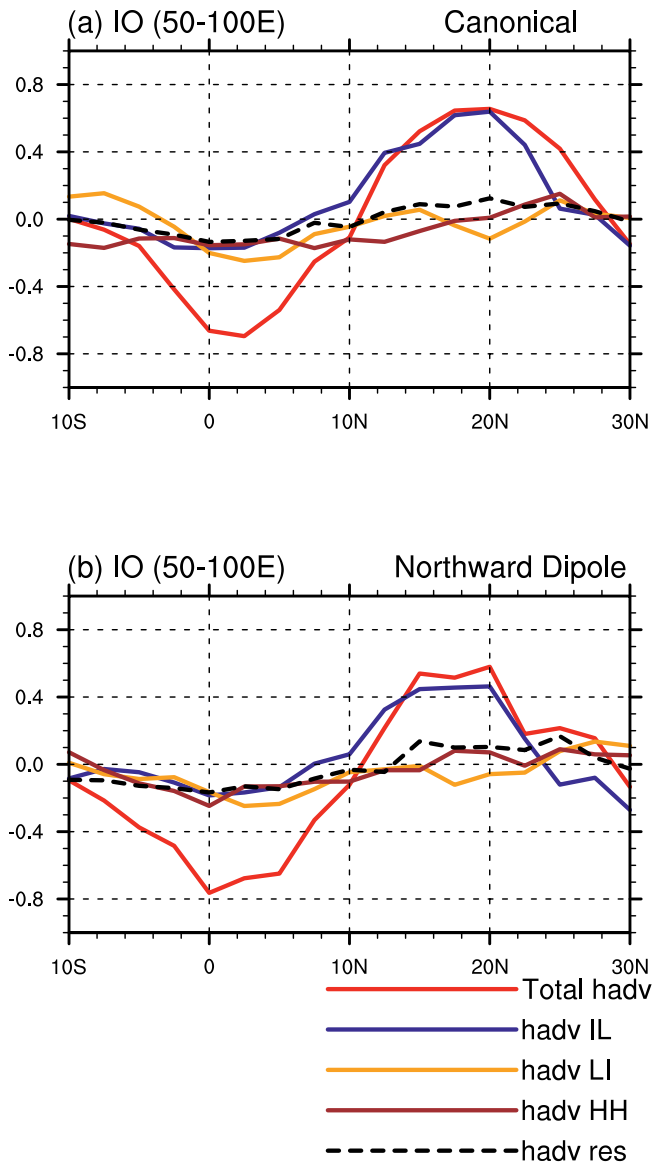


**Figure 4.** Different components of horizontal moisture advection over IO region (50°–100°E averaged) for the (a) canonical mode and (b) northward dipole mode. The red line denotes the total moisture advection, the blue line the advection of background (>90 days, denoted as L) moisture by intraseasonal (30–80 days, denoted as I) wind, the orange line the advection of intraseasonal moisture by background wind, the brown line the advection of high-frequency (<30 days, denoted as H) moisture by high-frequency wind, and the dashed black line the residual term. The residual term is obtained by subtracting the blue, orange, and brown lines from the red line.

#### 4.2. Northward Propagation of the Dipole Mode

For the northward dipole mode, there are positive (negative) moisture tendencies to the north of the IO (WP) enhanced (suppressed) convection (Figure 2b), signifying a dipolar northward propagation. However, the mechanisms for the northward propagation in the IO region and the WP region are different. In the IO region, the northward propagation mechanism is the same as the canonical mode. The positive tendencies to the north of the IO enhanced convection are dominated by the horizontal moisture advection (Figures 2e and 3c), which is attributed to the advection of background moisture by the zonal wind of the Rossby-wave response (Figure 4).

On the other hand, the negative moisture tendencies over the Philippine Sea, which signify the northward movement of the WP suppressed convection, are largely explained by the in-column process and evaporation (Figures 2h, 2k, and 3d). These negative in-column process and evaporation anomalies are associated with the underlying negative SST anomalies (Figure 7). The negative SST anomalies could induce negative surface evaporation anomalies and anomalous boundary layer divergence that leads to negative vertical moisture advection (in-column process) anomalies. Note that the generation of negative SST anomalies (Figure 7b) can be attributed to the Rossby-wave zonal winds in the previous pentads (pentad −2, Figure 7b), which induces positive evaporation anomalies (Figure 8) that cools the sea surface (Figure 7). Thus, it suggests that the northward propagation over WP is associated with the air-sea interaction, consistent with the previous results on the northward propagation mechanism of the ISO over the WNP (Hsu & Weng, 2001; Liu & Wang, 2014; B. Wang & Zhang, 2002; T. Wang, Yang, et al., 2018; Yang et al., 2020).

In the northward dipole mode, there are also positive moisture tendencies over the equatorial MC-WP region (Figure 2b). Why did not the positive tendency lead to eastward propagation? Note that these equatorial positive moisture tendencies are attributed to both the horizontal advection (Figure 2e) and the in-column process (Figure 2h). However, the horizontal moisture advection is located in the off-equatorial region, which tends to attenuate the suppressed convection over the northern WP rather than stimulate equatorial eastward propagation. On the other hand, the Kelvin-wave response is weak (Figure 2h), so the shallow and congestus convection and the associated low-level moistening are weak (Figure 6b) compared to the canonical mode, explaining why there is no eastward propagation of enhanced convection from the IO to MC in the dipole mode.

In short, the northward propagation of the convection anomalies over the IO in the northward dipole mode is driven by the same mechanism as that of the canonical mode, while the northward propagation of the convection anomalies over the WP is driven by the air-sea interaction.

#### 4.3. Eastward Expansion Mode

For the eastward expansion mode, there are positive moisture tendencies to the east of the enhanced convection, corresponding to the eastward propagation feature. The in-column process (Figure 2i) and surface evaporation (Figure 2l) are responsible for these positive moisture tendencies (Figure 3e). These positive in-column process and surface evaporation anomalies are associated with the Kelvin-wave easterly anomalies.



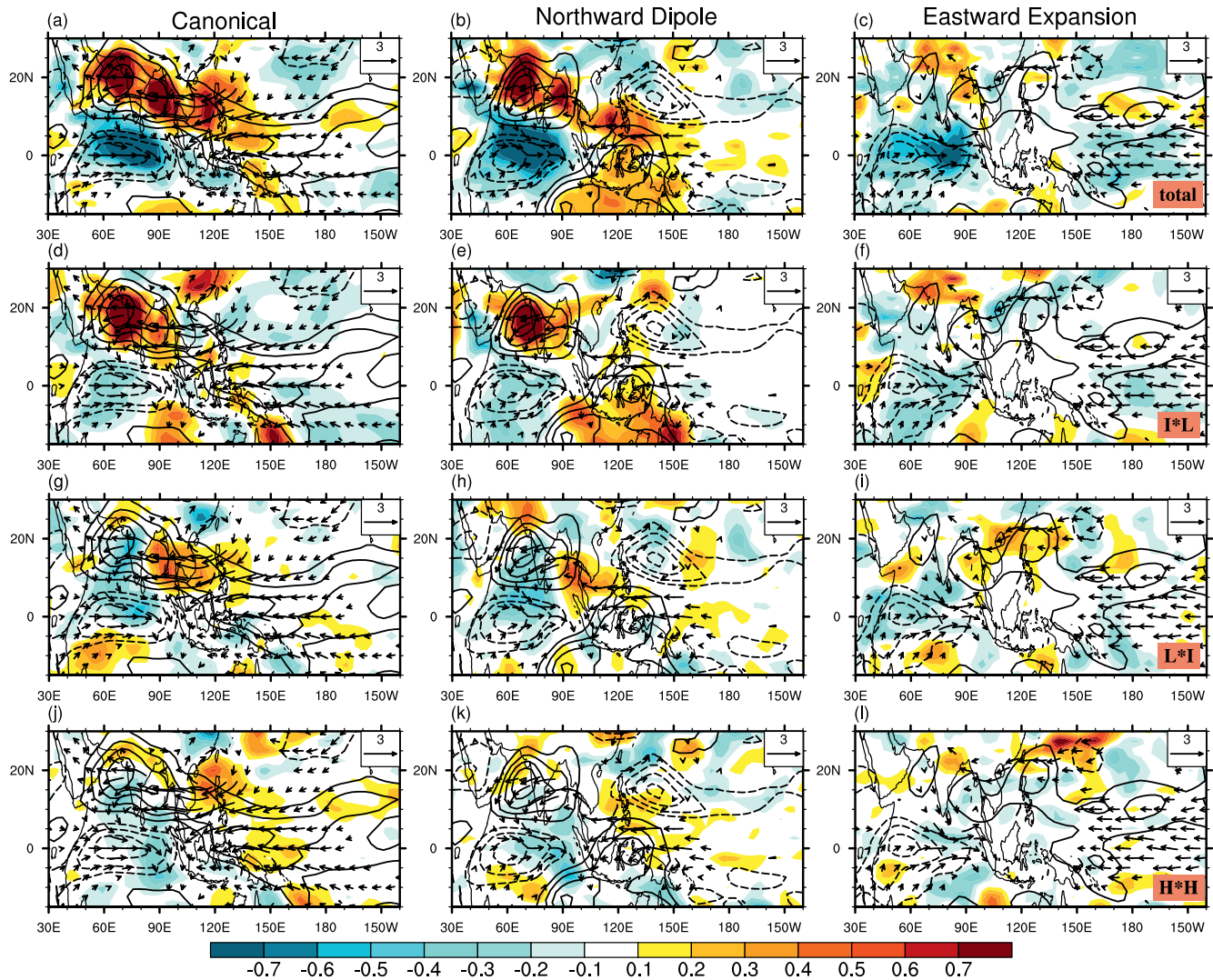


**Figure 5.** Spatial structures of different components of the horizontal moisture advection for the three BSISO modes. Shown are (first row) total horizontal moisture advection (shading, in unit of  $\text{kg m}^{-2} \text{day}^{-1}$ ), (second row) the advection of background moisture by intraseasonal wind, (third row) the advection of intraseasonal moisture by background wind, and (fourth row) the advection of high-frequency moisture by high-frequency wind. Also shown in each panel are the corresponding moisture tendency (contour with an interval of  $0.1 \text{ kg m}^{-2} \text{day}^{-1}$ ) and 850 hPa winds (vector, in unit of  $\text{m s}^{-1}$ ). The solid contour indicates positive value, the dashed contour indicates negative value, and the zero contour is omitted. The wind vectors are only shown for those above the 95% confidence level.

On the other hand, the positive moisture tendencies to the north of the enhanced convection are much weaker than those in the canonical mode and northward dipole mode, resulting in no apparent northward propagation of convection anomalies. This is due to the weak Rossby-wave zonal wind anomalies (Figure 1) and the associated weak horizontal moisture advection (Figure 2).

In short, the eastward propagation of the eastward expansion mode is driven by the Kelvin-wave response, while the weak Rossby-wave response leads to no apparent northward propagation.

## 5. Effects of Background Mean States

As the BSISO propagation diversity is attributed to the circulation differences, what causes these circulation differences? To seek the essential mechanism that might drive BSISO, we examine the effects of the background states, as the background states could affect the circulation features of the BSISO.

specific humidity & vertical velocity (10S-10N)

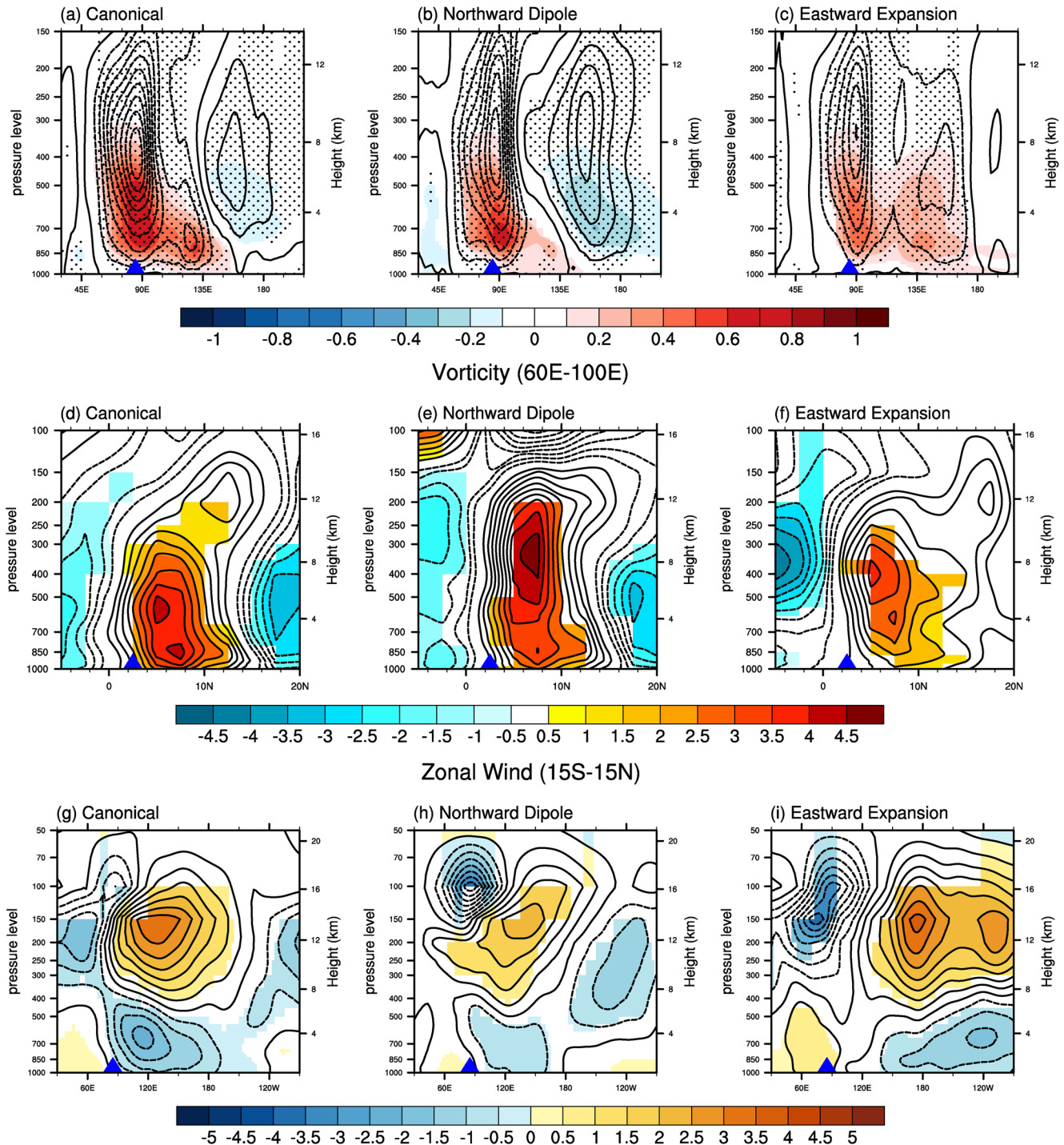


**Figure 6.** Vertical structure of the three BSISO modes. (a–c) show the equatorial (10°S–10°N averaged) specific humidity anomalies (shading, in units of  $\text{g kg}^{-1}$ ) and vertical velocity (contour with interval of  $0.35 \times 10^{-2} \text{ Pa s}^{-1}$ ); (d–f) show the vorticity (in units of  $10^{-6} \text{ s}^{-1}$ ) averaged from 60°E to 100°E; (g–i) show the zonal wind (in units of  $\text{m s}^{-1}$ ) averaged from 15°S to 15°N. The solid contour indicates positive value, the dashed contour indicates negative value, and the zero contour is omitted. The blue triangle denotes the center of enhanced IO convection. In (a–c), the specific humidity anomalies are only shown for those above 95% confidence level, and the region where vertical velocity anomalies are significant are stippled. In (d–i), the significant (above 95% level) area are shaded. For comparison, the vorticity anomalies in (d–f) and zonal wind anomalies in (g–i) are scaled to a minimal OLR value of  $-25 \text{ W m}^{-2}$  over the Indian Ocean region.



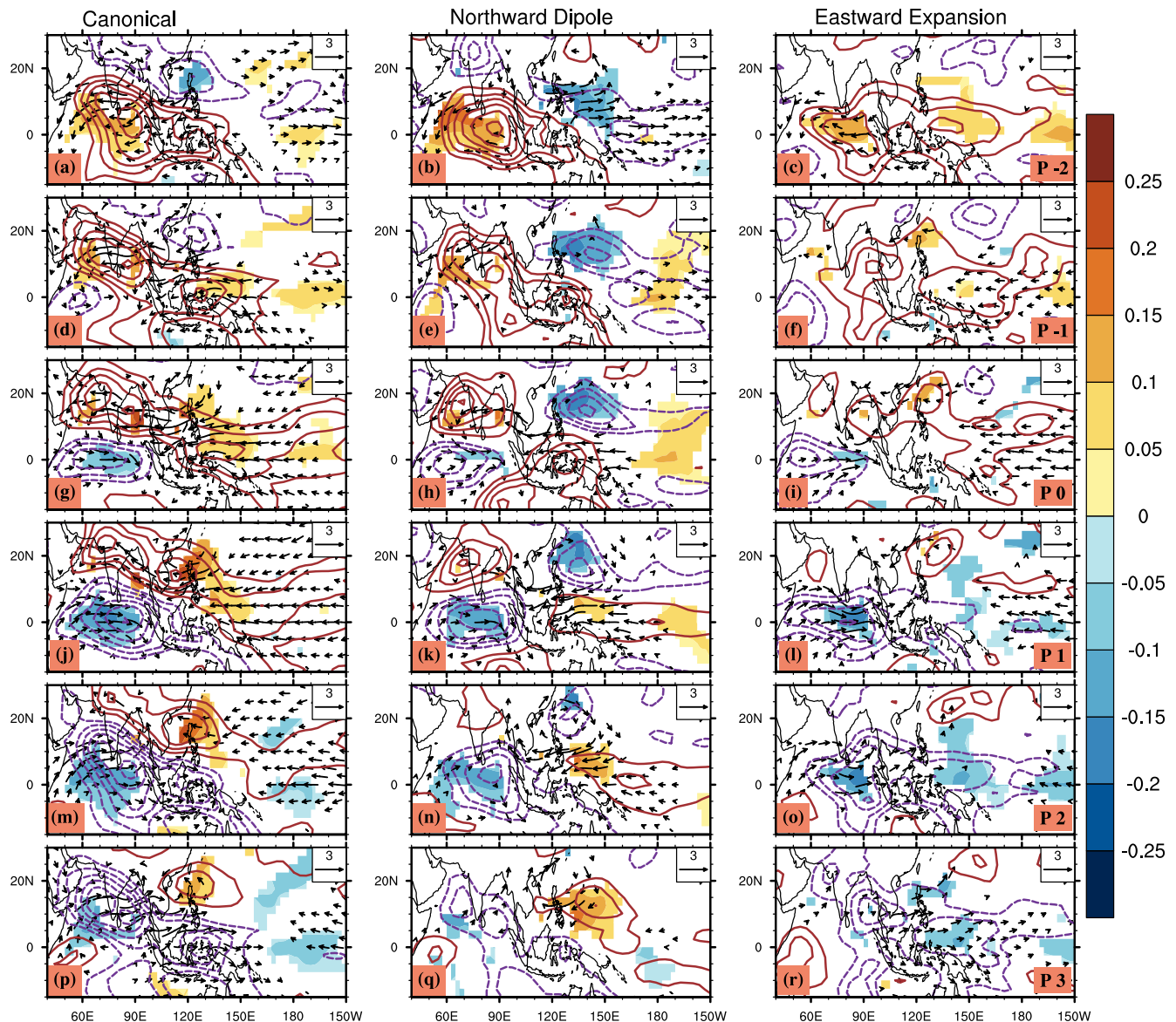


**Figure 7.** The evolution of SST anomalies associated with the three BSISO mode. The shading denotes the SST anomaly (in units of  $^{\circ}\text{C}$ ), the contour denotes the moisture tendency (contour with an interval of  $0.1 \text{ kg m}^{-2} \text{ day}^{-1}$ ), and the vector denotes the 850 hPa wind (in units of  $\text{m s}^{-1}$ ). The solid contour indicates positive value, the dashed contour indicates negative value, and the zero contour is omitted. The SST and wind anomalies are only shown for those above the 95% confidence level.

For the northward propagation, the winds of Rossby-wave response affect the moisture advection and air-sea interaction. What controls the strengths of the Rossby wave response? We speculate that the background circulation plays a salient role as the theory indicates that the background circulation can significantly affect the Rossby wave response (B. Wang & Xie, 1996; Xie & Wang, 1996).

The variation in the background circulation can be caused by the seasonal variation of the BSISO. To see this, Figures 9a–9c show the frequency distribution of the three BSISO modes. It reveals that the canonical mode tends to occur in May–June and the late summer season (September to October), the northward dipole mode prefers to occur in May to June, and the eastward propagating mode occurs dominantly in the transitional season (May and October). The  $\chi^2$  tests (Wilks, 2014) show that the frequency distributions of the three BSISO modes are significantly different from uniform distribution.

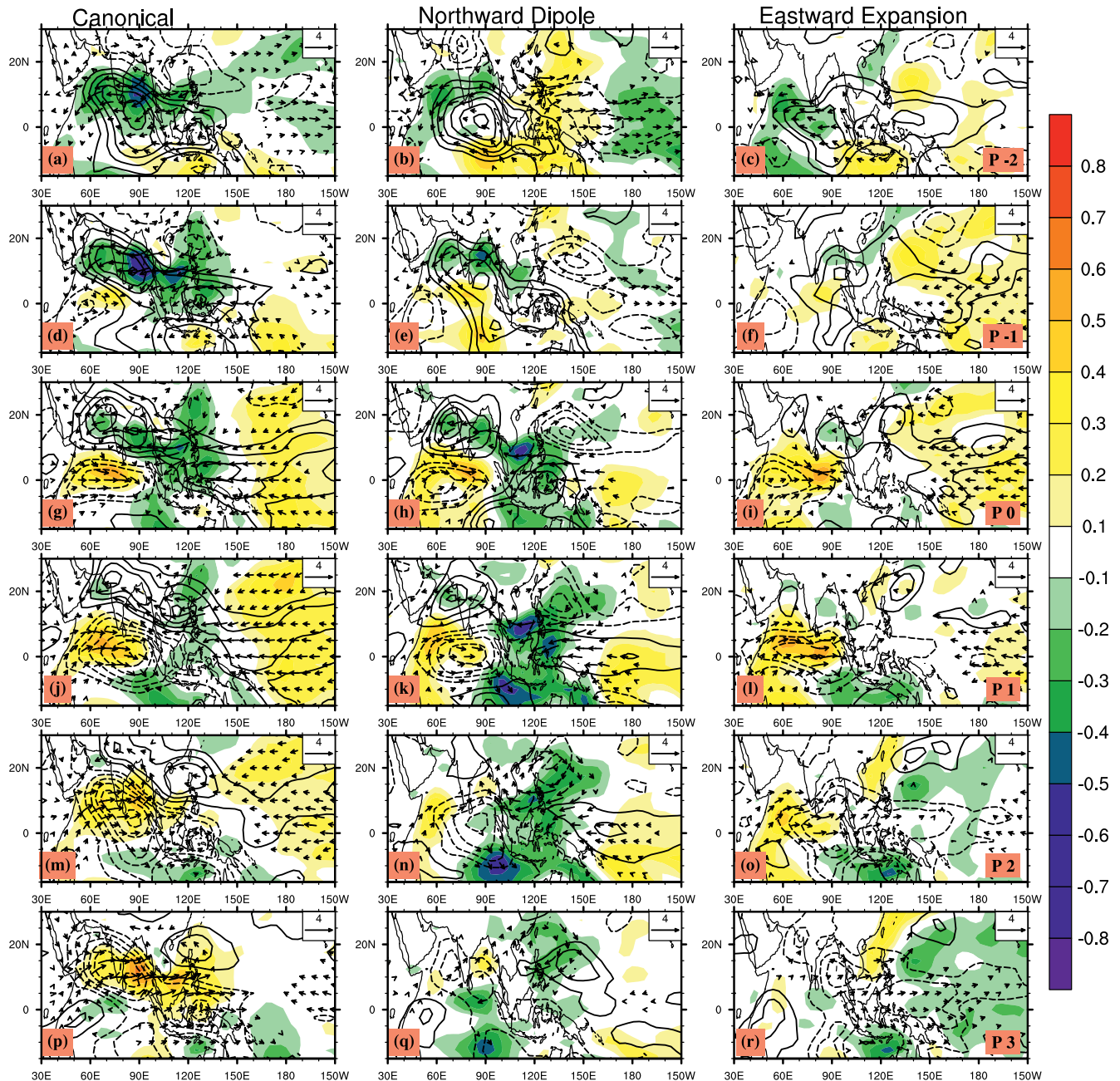
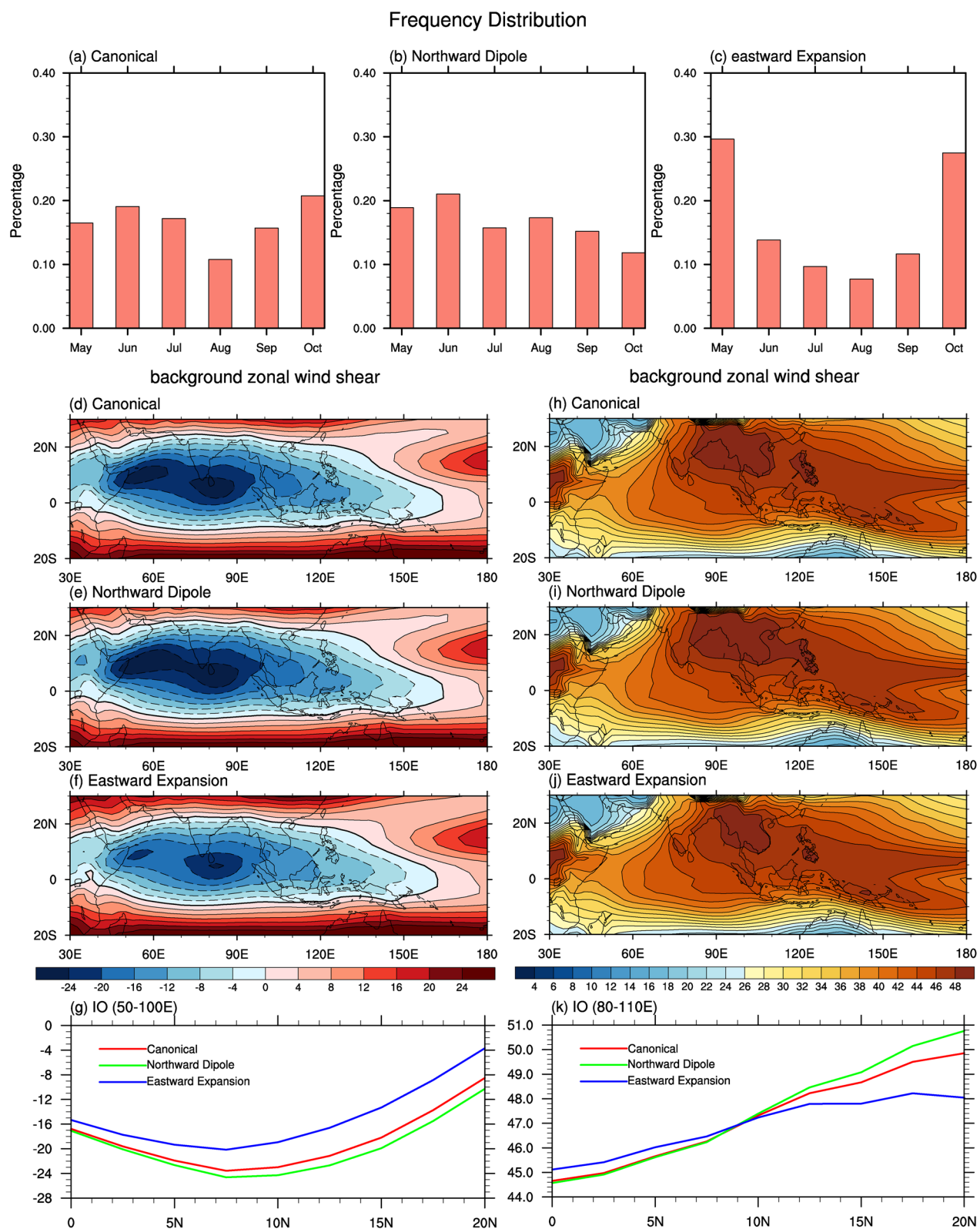


**Figure 8.** The evolution of surface evaporation anomalies associated with the three BSISO mode. The shading denotes the surface evaporation anomaly (in units of  $\text{kg m}^{-2} \text{day}^{-1}$ ), the contour denotes the moisture tendency (contour with an interval of  $0.1 \text{ kg m}^{-2} \text{day}^{-1}$ ), and the vector denotes the 850 hPa wind (in units of  $\text{m s}^{-1}$ ). The solid contour indicates positive value, the dashed contour indicates negative value, and the zero contour is omitted. The wind anomalies are only shown for those above the 95% confidence level.

As a consequence of seasonal dependence, the background circulation (Figures 9d–9g) exhibits salient differences between the modes having northward propagation (canonical mode and the northward dipole mode) and the eastward expansion mode. The northward dipole mode has the strongest background zonal easterly shear while the eastward expansion mode corresponds to the weakest easterly shear (Figure 9g). The maximum difference of the background zonal easterly shear over the IO (averaged between  $50^\circ\text{E}$  and  $100^\circ\text{E}$ ) is about  $6.7$  ( $5.1$ )  $\text{m s}^{-1}$  between the northward dipole (canonical) mode and eastward expansion mode. These differences in background zonal easterly shear (Figure 9g, solid lines) lead to stronger barotropic vorticity to the north of the IO enhanced convection in the northward dipole mode and canonical





mode (Figures 6d and 6e). The reason is that strong background zonal easterly shear favors enhancing the barotropic vorticity through coupling the baroclinic and barotropic modes and transferring energy from heating-generated baroclinic mode to barotropic mode (Drbohlav & Wang, 2005; Jiang et al., 2004; B. Wang, 2012; B. Wang & Xie, 1996, 1997; Yang et al., 2019). The enhanced barotropic vorticity explains why the Rossby-wave zonal wind anomalies to the north of the convection anomalies are stronger in the canonical mode and the northward dipole mode than the eastward expansion mode. The cyclonic barotropic vorticity to north of the convective center could also induce boundary layer moisture convergence, promoting northward propagation (Drbohlav & Wang, 2005; Jiang et al., 2004).

We also speculate that the variation in the background low-level moisture content (Jiang et al., 2018) may be another factor contributing to northward propagation, as the background moisture is the energy source for BSISO convection development and maintenance. The seasonal dependence of BSISO modes also affects the low-level background moisture distributions. Figures 9h–9k show that the northward dipole and canonical BSISO modes have higher background low-level moisture content over South Asia (80°–110°E) than the eastward expansion mode. The high background moisture enhances the westward moisture advection when the Rossby-wave easterly anomalies are prevalent, thereby promoting the northward propagation of BSISO convection anomalies in the IO.

Why is the Kelvin-wave response so weak in the northward dipole mode that eastward propagation is absent? Figures 6g–6i show that the zonal extent of the Kelvin-wave response (measured by the equatorial zonal wind) in the northward dipole mode is considerably shorter than those in the other two BSISO modes. A smaller zonal scale leads to a weak Kelvin-wave interaction with the boundary layer convergence (G. Chen & Wang, 2019). Thus, the Kelvin-wave response in the northward dipole mode is weak. Moreover, the background moisture has prominent meridional asymmetry about the equator in the northward dipole mode (Figure 9k), which is not favorable for the development of the equatorial symmetric component (such as the Kelvin-wave response). These two factors conspire to suppress the development of Kelvin-wave response in the northward dipole mode, prohibiting its eastward propagation.

## 6. Concluding Remarks

By using 2-D cluster analysis, the BSISO has been classified objectively into three archetypes: the northeastward propagating (canonical) mode, the northward propagating seesaw dipole mode, and the eastward expansion mode. Each BSISO mode shows distinct circulation structure. The BSISO modes having northward propagation (the northward dipole mode and canonical mode) have stronger Rossby-wave zonal winds to the north of the convection anomalies than the BSISO mode without northward propagation (the eastward expansion mode). The BSISO modes with eastward propagation (the canonical mode and the eastward expansion mode) have stronger Kelvin-wave responses to the east of the convection anomalies than the BSISO mode without eastward propagation (the northward dipole mode). A strong Rossby wave response leads to northward propagation of convection by moistening the atmosphere to the north via advecting the low-level background moisture (in the IO region) and through air-sea interaction (in the WP region). A strong Kelvin-wave response leads to eastward propagation by moistening to the east via enhancing the in-column process (net vertical moistening due to convection and large-scale dynamics) and surface latent heat flux (evaporation).

The results here extend the conclusion of previous studies (B. Wang et al., 2019; B. Wang & Lee, 2017) from boreal winter to boreal summer that the diversity of circulation structures signify diverse ISO propagation. These results also potentially provide precursors for foreseeing BSISO propagation. For example, a strong Kelvin-wave component to the east of the convection center suggests subsequent eastward propagation of

**Figure 9.** Different seasonal dependence of the occurrence for the three BSISO modes and the corresponding background states. (a–c) show the frequency distributions of the three BSISO modes; (d–f) show the associated vertical shear of background zonal wind (defined as  $U_{200}-U_{850}$ , in units of  $m\ s^{-1}$ ) and (g) their averaged values over 50°–100°E; (h–j) show the low-level (1,000–600 hPa integrated) background specific humidity (in units of  $kg\ m^{-2}$ ) distribution and (k) their averaged values over 80°–110°E. The frequency distribution for a particular month is calculated as the number of days when the BSISO events (only the period from day –7 to day 17 is counted) occur in that month. The background states are obtained as a weighted mean of MJJASO monthly data with the weights being the frequencies shown in (a–c). The thin solid contour indicates positive value, the thin dashed contour indicates negative value, and thick solid contour is the zero contour.

the convection center, while a strong Rossby-wave component to the north suggests subsequent northward propagation.

The diverse circulation structures are affected by the variation of the background state, explained by distinct seasonal dependences associated with different BSISO modes. The eastward expansion BSISO occurs dominantly in the transitional season (May and October), while the northward dipole BSISO and the canonical BSISO have peaks during June. In the northward dipole and canonical modes, strong background zonal easterly shear occurs over the IO, resulting in a strong Rossby wave response. Moreover, the background low-level moisture distributions are more equatorially asymmetric in these two modes. The strong Rossby wave response and large meridional asymmetry in the background moisture distribution conspire to promote northward propagation over the IO in these two BSISO modes through enhancing the horizontal moisture advection. On the other hand, the northward dipole BSISO is a convectively coupled system with a relatively short zonal scale and occurs in a more meridionally asymmetric environment. These conditions lead to weak or even absent Kelvin-wave response in the northward dipole BSISO, forbidding its eastward propagation.

In short, this study objectively and systematically identified three types BSISO modes with distinct two-dimensional propagation features. The diverse propagation features are attributed to the BSISO circulation structural differences, which are caused by the variations in the season-dependent background states.

It is interesting to ask whether other forcings could induce background state variation. For example, B. Wang et al. (2019) have shown that the El Niño-Southern Oscillation (ENSO) and the associated changes of background SST could regulate the propagation of boreal winter MJO through modifying the background states. It is found that the three BSISO modes are not closely connected to the background SST change associated low-frequency climate modes, such as ENSO or Indian Ocean dipole.

We used the equatorial IO as a reference location for selecting the BSISO events in this work. The reason is that the equatorial IO is a prevailing origin for the BSISO (Lau & Chan, 1986). Using other reference locations will have similar results. We have tested the SCS-WP region (110°E–140°E, 5°N–15°N) as a reference location, the similar three BSISO clusters are found, except that the eastward expansion BSISO is more off-equatorially located. We have also done analysis on four clusters. It shows that the northward dipole mode and the eastward expansion mode are also obtained in the four-cluster results, while the canonical mode splits into two modes with very similar propagation patterns, which may not be physically separable. Therefore, the three archetypes of BSISO found here are significant and representative.

In this study, the OLR is used as proxy of convection for cluster analysis. We have also performed cluster analysis on TRMM precipitation data for period of 1998–2018. The results revealed that there are only two modes identified in the precipitation data, that is, the canonical mode and the northward dipole mode, while the eastward expansion mode is absent, contrasting to the OLR results. A possible explanation is that precipitation and OLR have different features in the stratiform zone. If the convection activity is characterized by large area of stratiform clouds with light amount of precipitation, the OLR signals will be relatively strong while the precipitation signals will be relatively weak. This seems to be the case for the eastward expansion mode, which has stronger stratiform convection, as suggested by Figures 6a–6c that the level of maximum vertical velocity is higher in this mode (around 300 hPa) than the other two modes (around 400 hPa). Thus, in the precipitation data, the eastward expansion mode is hard to be distinguished from other modes, while in the OLR data it can be distinguished as an independent mode.

The findings here suggest that different BSISO events would have distinct impacts on global weather and systems. It would be interesting to find out how different BSISO affect the global monsoon systems, tropical cyclones, extreme weather events, and others. The knowledge obtained here may explain why some models do not adequately simulate the northward propagation of the BSISO over the Asian monsoonal regions. It would be of interest to determine how the global climate models in the Coupled Model Intercomparison Project Phase 6 capture the BSISO propagation diversity, and how the BSISO diversity changes in the future under global warming.

## Data Availability Statement

The ERA-interim data are available at <https://apps.ecmwf.int/datasets/>. The OLR data are available at [https://www.esrl.noaa.gov/psd/data/gridded/data.interp\\_OLR.html](https://www.esrl.noaa.gov/psd/data/gridded/data.interp_OLR.html).

## Acknowledgments

GC is supported by the National Natural Science Foundation of China (Grant 2081011900501) and the Nature Science Foundation of the Jiangsu Higher Education Institutions of China (Grant 1421011901005). BW is supported by the National Science Foundation (Climate Dynamics Division) Award # AGS-1540783 and the National Natural Science Foundation of China (Grant No. 91437218). This paper is the IPRC publication #1515, SOEST publication # 11311, and ESMC publication #346.

## References

- Adames, Á. F. (2017). Precipitation budget of the Madden-Julian oscillation. *Journal of the Atmospheric Sciences*, 74(6), 1799–1817. <https://doi.org/10.1175/jas-d-16-0242.1>
- Adames, Á. F., Wallace, J. M., & Monteiro, J. M. (2016). Seasonality of the structure and propagation characteristics of the MJO. *Journal of the Atmospheric Sciences*, 73(9), 3511–3526. <https://doi.org/10.1175/jas-d-15-0232.1>
- Ajayamohan, R. S., Annamalai, H., Luo, J.-J., Hafner, J., & Yamagata, T. (2011). Poleward propagation of boreal summer intraseasonal oscillations in a coupled model: Role of internal processes. *Climate Dynamics*, 37(5), 851–867. <https://doi.org/10.1007/s00382-010-0839-6>
- Annamalai, H. (2010). Moist dynamical linkage between the equatorial Indian Ocean and the South Asian monsoon trough\*. *Journal of the Atmospheric Sciences*, 67(3), 589–610. <https://doi.org/10.1175/2009jas2991.1>
- Bretherton, C. S., Peters, M. E., & Back, L. E. (2004). Relationships between water vapor path and precipitation over the tropical oceans. *Journal of Climate*, 17(7), 1517–1528. [https://doi.org/10.1175/1520-0442\(2004\)017<1517:rbwvpa>2.0.co;2](https://doi.org/10.1175/1520-0442(2004)017<1517:rbwvpa>2.0.co;2)
- Chen, G., & Wang, B. (2018). Effects of enhanced front Walker cell on the eastward propagation of the MJO. *Journal of Climate*, 31(19), 7719–7738. <https://doi.org/10.1175/jcli-d-17-0383.1>
- Chen, G., & Wang, B. (2019). Dynamic moisture mode versus moisture mode in MJO dynamics: Importance of the wave feedback and boundary layer convergence feedback. *Climate Dynamics*, 52, 5127–5143. <https://doi.org/10.1007/s00382-018-4433-7>
- Chen, G., & Wang, B. (2020). Circulation factors determining the propagation speed of the Madden-Julian oscillation. *Journal of Climate*, 33(8), 3367–3380. <https://doi.org/10.1175/jcli-d-19-0661.1>
- Chen, T.-C., & Murakami, M. (1988). The 30–50 day variation of convective activity over the Western Pacific Ocean with emphasis on the Northwestern region. *Monthly Weather Review*, 116(4), 892–906. [https://doi.org/10.1175/1520-0493\(1988\)116<0892:Tdvoca>2.0.Co;2](https://doi.org/10.1175/1520-0493(1988)116<0892:Tdvoca>2.0.Co;2)
- Chen, T.-C., Yen, M.-C., & Weng, S.-P. (2000). Interaction between the summer monsoons in east Asia and the South China sea: Intraseasonal monsoon modes. *Journal of the Atmospheric Sciences*, 57(9), 1373–1392. [https://doi.org/10.1175/1520-0469\(2000\)057<1373:Ibtsmi>2.0.Co;2](https://doi.org/10.1175/1520-0469(2000)057<1373:Ibtsmi>2.0.Co;2)
- Dee, D. P., Uppala, S. M., Simmons, A. J., Berrisford, P., Poli, P., Kobayashi, S., et al. (2011). The ERA-Interim reanalysis: Configuration and performance of the data assimilation system. *Quarterly Journal of the Royal Meteorological Society*, 137(656), 553–597. <https://doi.org/10.1002/qj.828>
- DeMott, C. A., Stan, C., & Randall, D. A. (2013). Northward propagation mechanisms of the boreal summer intraseasonal oscillation in the ERA-interim and SP-CCSM. *Journal of Climate*, 26(6), 1973–1992. <https://doi.org/10.1175/jcli-d-12-00191.1>
- Drbohlav, H.-K. L., & Wang, B. (2005). Mechanism of the northward-propagating intraseasonal oscillation: Insights from a zonally symmetric model\*. *Journal of Climate*, 18(7), 952–972. <https://doi.org/10.1175/jcli3306.1>
- Duchon, C. E. (1979). Lanczos filtering in one and two dimensions. *Journal of Applied Meteorology*, 18(8), 1016–1022. [https://doi.org/10.1175/1520-0450\(1979\)018<1016:LFIOTAT>2.0.CO;2](https://doi.org/10.1175/1520-0450(1979)018<1016:LFIOTAT>2.0.CO;2)
- Gill, A. E. (1980). Some simple solutions for heat-induced tropical circulation. *Quarterly Journal of the Royal Meteorological Society*, 106(449), 447–462. <https://doi.org/10.1002/qj.49710644905>
- Goswami, B. (2012). South Asian monsoon. In *Intraseasonal variability in the atmosphere-ocean climate system* (2nd ed.).
- Goswami, B. N., Ajayamohan, R. S., Xavier, P. K., & Sengupta, D. (2003). Clustering of synoptic activity by Indian summer monsoon intraseasonal oscillations. *Geophysical Research Letters*, 30(8). <https://doi.org/10.1029/2002gl016734>
- Goswami, B. N., & Xavier, P. K. (2003). Potential predictability and extended range prediction of Indian summer monsoon breaks. *Geophysical Research Letters*, 30(18). <https://doi.org/10.1029/2003gl017810>
- Hendon, H. H., & Salby, M. L. (1994). The life cycle of the Madden-Julian Oscillation. *Journal of the Atmospheric Sciences*, 51(15), 2225–2237. [https://doi.org/10.1175/1520-0469\(1994\)051<2225:TLCOTM>2.0.CO;2](https://doi.org/10.1175/1520-0469(1994)051<2225:TLCOTM>2.0.CO;2)
- Hsu, H.-H., & Weng, C.-H. (2001). Northwestward propagation of the intraseasonal oscillation in the western North Pacific during the Boreal summer: Structure and mechanism. *Journal of Climate*, 14(18), 3834–3850. [https://doi.org/10.1175/1520-0442\(2001\)014<3834:Npotio>2.0.Co;2](https://doi.org/10.1175/1520-0442(2001)014<3834:Npotio>2.0.Co;2)
- Jiang, X. (2017). Key processes for the eastward propagation of the Madden-Julian Oscillation based on multimodel simulations. *Journal of Geophysical Research: Atmospheres*, 122(2), 755–770. <https://doi.org/10.1002/2016jd025955>
- Jiang, X., Adames, Á. F., Zhao, M., Waliser, D., & Maloney, E. (2018). A unified moisture mode framework for seasonality of the Madden-Julian Oscillation. *Journal of Climate*, 31(11), 4215–4224. <https://doi.org/10.1175/jcli-d-17-0671.1>
- Jiang, X., Li, T., & Wang, B. (2004). Structures and mechanisms of the northward propagating boreal summer intraseasonal oscillation\*. *Journal of Climate*, 17(5), 1022–1039. [https://doi.org/10.1175/1520-0442\(2004\)017<1022:samotn>2.0.co;2](https://doi.org/10.1175/1520-0442(2004)017<1022:samotn>2.0.co;2)
- Jiang, X., Maloney, E., & Su, H. (2020). Large-scale controls of propagation of the Madden-Julian Oscillation. *Climate and Atmospheric Science*, 3(1), 29. <https://doi.org/10.1038/s41612-020-00134-x>
- Kaufman, L., & Rousseeuw, P. J. (2009). Finding groups in data: An introduction to cluster analysis (Vol. 344). John Wiley & Sons.
- Kemball-Cook, S., & Wang, B. (2001). Equatorial waves and air-sea interaction in the boreal summer intraseasonal oscillation. *Journal of Climate*, 14(13), 2923–2942. [https://doi.org/10.1175/1520-0442\(2001\)014<2923:ewaasi>2.0.co;2](https://doi.org/10.1175/1520-0442(2001)014<2923:ewaasi>2.0.co;2)
- Kikuchi, K., Wang, B., & Kajikawa, Y. (2012). Bimodal representation of the tropical intraseasonal oscillation. *Climate Dynamics*, 38(9–10), 1989–2000. <https://doi.org/10.1007/s00382-011-1159-1>
- Kim, D., Kim, H., & Lee, M. I. (2017). Why does the MJO detour the maritime continent during austral summer? *Geophysical Research Letters*, 44(5), 2579–2587. <https://doi.org/10.1002/2017gl072643>
- Kim, D., Kug, J.-S., & Sobel, A. H. (2014). Propagating versus nonpropagating Madden-Julian Oscillation events. *Journal of Climate*, 27(1), 111–125. <https://doi.org/10.1175/JCLI-D-13-00084.1>
- Krishnamurthy, V., & Shukla, J. (2000). Intraseasonal and interannual variability of rainfall over India. *Journal of Climate*, 13(24), 4366–4377. [https://doi.org/10.1175/1520-0442\(2000\)013<0001:laivor>2.0.Co;2](https://doi.org/10.1175/1520-0442(2000)013<0001:laivor>2.0.Co;2)
- Krishnamurti, T. N., & Subrahmanyam, D. (1982). The 30–50 day Mode at 850 mb during MONEX. *Journal of the Atmospheric Sciences*, 39(9), 2088–2095. [https://doi.org/10.1175/1520-0469\(1982\)039<2088:TDMAMD>2.0.CO;2](https://doi.org/10.1175/1520-0469(1982)039<2088:TDMAMD>2.0.CO;2)



- Lau, K.-M., & Chan, P. H. (1986). Aspects of the 40–50 day oscillation during the Northern summer as inferred from outgoing longwave radiation. *Monthly Weather Review*, 114(7), 1354–1367. [https://doi.org/10.1175/1520-0493\(1986\)114<1354:Aotdod>2.0.Co;2](https://doi.org/10.1175/1520-0493(1986)114<1354:Aotdod>2.0.Co;2)
- Lau, K.-M., & Peng, L. (1990). Origin of low frequency (intraseasonal) oscillations in the tropical atmosphere. Part III: monsoon dynamics. *Journal of the Atmospheric Sciences*, 47(12), 1443–1462. [https://doi.org/10.1175/1520-0469\(1990\)047<1443:Oolfoi>2.0.Co;2](https://doi.org/10.1175/1520-0469(1990)047<1443:Oolfoi>2.0.Co;2)
- Lawrence, D. M., & Webster, P. J. (2002). The boreal summer intraseasonal oscillation: Relationship between northward and eastward movement of convection. *Journal of the Atmospheric Sciences*, 59(9), 1593–1606. [https://doi.org/10.1175/1520-0469\(2002\)059<1593:Tbsior>2.0.Co;2](https://doi.org/10.1175/1520-0469(2002)059<1593:Tbsior>2.0.Co;2)
- Lee, J.-Y., Wang, B., Wheeler, M. C., Fu, X., Waliser, D. E., & Kang, I.-S. (2013). Real-time multivariate indices for the boreal summer intraseasonal oscillation over the Asian summer monsoon region. *Climate Dynamics*, 40(1), 493–509. <https://doi.org/10.1007/s00382-012-1544-4>
- Lee, S.-S., Wang, B., Waliser, D. E., Neena, J. M., & Lee, J.-Y. (2015). Predictability and prediction skill of the boreal summer intraseasonal oscillation in the Intraseasonal Variability Hindcast Experiment. *Climate Dynamics*, 45, 2123–2135.
- Li, T. (2014). Recent advance in understanding the dynamics of the Madden-Julian Oscillation. *Acta Meteorologica Sinica*, 28(1), 1–33. <https://doi.org/10.1007/s13351-014-3087-6>
- Liebmann, B., & Smith, C. (1996). Description of a complete (interpolated) outgoing longwave radiation data set. *Bulletin of the American Meteorological Society*, 77, 1275–1277.
- Liu, F., & Wang, B. (2014). A mechanism for explaining the maximum intraseasonal oscillation center over the western North Pacific\*. *Journal of Climate*, 27(2), 958–968. <https://doi.org/10.1175/jcli-d-12-00797.1>
- Madden, R. A. (1986). Seasonal variations of the 40–50 day oscillation in the tropics. *Journal of the Atmospheric Sciences*, 43(24), 3138–3158. [https://doi.org/10.1175/1520-0469\(1986\)043<3138:SVOTDO>2.0.CO;2](https://doi.org/10.1175/1520-0469(1986)043<3138:SVOTDO>2.0.CO;2)
- Madden, R. A., & Julian, P. R. (1971). Detection of a 40–50 day oscillation in the zonal wind in the tropical Pacific. *Journal of the Atmospheric Sciences*, 28(5), 702–708. [https://doi.org/10.1175/1520-0469\(1971\)028<0702:DOADOI>2.0.CO;2](https://doi.org/10.1175/1520-0469(1971)028<0702:DOADOI>2.0.CO;2)
- Madden, R. A., Julian, P. R. (1972). Description of global-scale circulation cells in the tropics with a 40–50 day period. *Journal of the Atmospheric Sciences*, 29(6), 1109–1123. [https://doi.org/10.1175/1520-0469\(1972\)029<1109:DOGCC>2.0.CO;2](https://doi.org/10.1175/1520-0469(1972)029<1109:DOGCC>2.0.CO;2)
- Maloney, E. D. (2009). The moist static energy budget of a composite tropical intraseasonal oscillation in a climate model. *Journal of Climate*, 22(3), 711–729. <https://doi.org/10.1175/2008JCLI2542.1>
- Maloney, E. D., & Hartmann, D. L. (1998). Frictional moisture convergence in a composite life cycle of the Madden-Julian Oscillation. *Journal of Climate*, 11(9), 2387–2403. [https://doi.org/10.1175/1520-0442\(1998\)011<2387:FMCIAC>2.0.CO;2](https://doi.org/10.1175/1520-0442(1998)011<2387:FMCIAC>2.0.CO;2)
- Matthews, A. J., Hoskins, B. J., & Masutani, M. (2004). The global response to tropical heating in the Madden-Julian Oscillation during the northern winter. *Quarterly Journal of the Royal Meteorological Society*, 130(601), 1991–2011. <https://doi.org/10.1256/qj.02.123>
- Moon, J.-Y., Wang, B., Lee, S.-S., & Ha, K.-J. (2018). An intraseasonal genesis potential index for tropical cyclones during Northern Hemisphere summer. *Journal of Climate*, 31(22), 9055–9071. <https://doi.org/10.1175/jcli-d-18-0515.1>
- Murakami, T., Nakazawa, T., & He, J. (1984). On the 40–50 day oscillations during the 1979 Northern Hemisphere Summer. *Journal of the Meteorological Society of Japan*, 62(3), 469–484. [https://doi.org/10.2151/jmsj1965.62.3\\_469](https://doi.org/10.2151/jmsj1965.62.3_469)
- Nakazawa, T. (1986). Intraseasonal variations of OLR in the tropics during the FGGE year. *Journal of the Meteorological Society of Japan*, 64(1), 17–34. [https://doi.org/10.2151/jmsj1965.64.1\\_17](https://doi.org/10.2151/jmsj1965.64.1_17)
- Naumann, G., & Vargas, W. M. (2010). Joint diagnostic of the surface air temperature in southern South America and the Madden-Julian Oscillation. *Weather and Forecasting*, 25(4), 1275–1280. <https://doi.org/10.1175/2010WAF2222418.1>
- Neena, J. M., Lee, J. Y., Waliser, D., Wang, B., & Jiang, X. (2014). Predictability of the Madden-Julian Oscillation in the intraseasonal variability hindcast experiment (ISVHE)\*. *Journal of Climate*, 27(12), 4531–4543. <https://doi.org/10.1175/JCLI-D-13-00624.1>
- Neena, J., Waliser, D., & Jiang, X. (2017). Model performance metrics and process diagnostics for boreal summer intraseasonal variability. *Climate Dynamics*, 48(5–6), 1661–1683. <https://doi.org/10.1007/s00382-016-3166-8>
- Parthasarathy, B., & Mooley, D. A. (1978). Some features of a long homogeneous series of Indian summer monsoon rainfall. *Monthly Weather Review*, 106(6), 771–781. [https://doi.org/10.1175/1520-0493\(1978\)106<0771:Sfoalh>2.0.Co;2](https://doi.org/10.1175/1520-0493(1978)106<0771:Sfoalh>2.0.Co;2)
- Pillai, P. A., & Sahai, A. K. (2016). Moisture dynamics of the northward and eastward propagating boreal summer intraseasonal oscillations: Possible role of tropical Indo-West Pacific SST and circulation. *Climate Dynamics*, 47(3), 1335–1350. <https://doi.org/10.1007/s00382-015-2904-7>
- Salby, M. L., Garcia, R. R., & Hendon, H. H. (1994). Planetary-scale circulations in the presence of climatological and wave-induced heating. *Journal of the Atmospheric Sciences*, 51(16), 2344–2367. [https://doi.org/10.1175/1520-0469\(1994\)051<2344:PSCITP>2.0.CO;2](https://doi.org/10.1175/1520-0469(1994)051<2344:PSCITP>2.0.CO;2)
- Sikka, D. R., & Gadgil, S. (1980). On the maximum cloud zone and the ITCZ over Indian, longitudes during the Southwest monsoon. *Monthly Weather Review*, 108(11), 1840–1853. [https://doi.org/10.1175/1520-0493\(1980\)108<1840:Otmcza>2.0.Co;2](https://doi.org/10.1175/1520-0493(1980)108<1840:Otmcza>2.0.Co;2)
- Wang, B. (2012). Theory. In W. K. M. Lau, & D. E. Waliser (Eds.), *Intraseasonal variability in the atmosphere-ocean climate system* (2nd ed., pp. 335–398). Springer.
- Wang, B., Chen, G., & Liu, F. (2019). Diversity of the Madden-Julian Oscillation. *Science Advances*, 5(7), eaax0220. <https://doi.org/10.1126/sciadv.aax0220>
- Wang, B., & Lee, S.-S. (2017). MJO propagation shaped by zonal asymmetric structures: Results from 24 GCM simulations. *Journal of Climate*, 30(19), 7933–7952. <https://doi.org/10.1175/jcli-d-16-0873.1>
- Wang, B., Lee, S.-S., Waliser, D. E., Zhang, C., Sobel, A., Maloney, E., et al. (2018). Dynamics-oriented diagnostics for the Madden-Julian Oscillation. *Journal of Climate*, 31(8), 3117–3135. <https://doi.org/10.1175/jcli-d-17-0332.1>
- Wang, B., & Rui, H. (1990). Synoptic climatology of transient tropical intraseasonal convection anomalies: 1975–1985. *Meteorology and Atmospheric Physics*, 44(1–4), 43–61. <https://doi.org/10.1007/bf01026810>
- Wang, B., & Xie, X. (1996). Low-frequency equatorial waves in vertically sheared zonal flow. Part I: Stable waves. *Journal of the Atmospheric Sciences*, 53(3), 449–467. [https://doi.org/10.1175/1520-0469\(1996\)053<0449:LFEWIV>2.0.CO;2](https://doi.org/10.1175/1520-0469(1996)053<0449:LFEWIV>2.0.CO;2)
- Wang, B., & Xie, X. (1997). A model for the boreal summer intraseasonal oscillation. *Journal of the Atmospheric Sciences*, 54(1), 72–86. [https://doi.org/10.1175/1520-0469\(1997\)054<0072:AMFTBS>2.0.CO;2](https://doi.org/10.1175/1520-0469(1997)054<0072:AMFTBS>2.0.CO;2)
- Wang, B., & Zhang, Q. (2002). Pacific-East Asian teleconnection. Part II: How the Philippine Sea anomalous anticyclone is established during El Niño development\*. *Journal of Climate*, 15(22), 3252–3265. [https://doi.org/10.1175/1520-0442\(2002\)015<3252:Peatpi>2.0.CO;2](https://doi.org/10.1175/1520-0442(2002)015<3252:Peatpi>2.0.CO;2)
- Wang, L., & Li, T. (2020). Re-examining the MJO moisture mode theories with normalized phase evolutions. *Journal of Climate*, 33(19), 8523–8536. <https://doi.org/10.1175/jcli-d-20-0202.1>
- Wang, T., Yang, X.-Q., Fang, J., Sun, X., & Ren, X. (2018). Role of air-sea interaction in the 30–60 day boreal summer intraseasonal oscillation over the western North Pacific. *Journal of Climate*, 31(4), 1653–1680. <https://doi.org/10.1175/jcli-d-17-0109.1>

- Wheeler, M. C., & Hendon, H. H. (2004). An all-season real-time multivariate MJO index: Development of an index for monitoring and prediction. *Monthly Weather Review*, 132(8), 1917–1932. [https://doi.org/10.1175/1520-0493\(2004\)132<1917:AARMMI>2.0.CO;2](https://doi.org/10.1175/1520-0493(2004)132<1917:AARMMI>2.0.CO;2)
- Wilks, D. (2014). *Statistical methods in the atmospheric sciences*. Elsevier.
- Xie, X., & Wang, B. (1996). Low-frequency equatorial waves in vertically sheared zonal flow. Part II: Unstable waves. *Journal of the Atmospheric Sciences*, 53(23), 3589–3605. [https://doi.org/10.1175/1520-0469\(1996\)053<3589:LFEWIV>2.0.CO;2](https://doi.org/10.1175/1520-0469(1996)053<3589:LFEWIV>2.0.CO;2)
- Yanai, M., Esbensen, S., & Chu, J.-H. (1973). Determination of bulk properties of tropical cloud clusters from large-scale heat and moisture budgets. *Journal of the Atmospheric Sciences*, 30(4), 611–627. [https://doi.org/10.1175/1520-0469\(1973\)030<0611:Dobpot>2.0.Co;2](https://doi.org/10.1175/1520-0469(1973)030<0611:Dobpot>2.0.Co;2)
- Yang, Y.-M., Lee, J.-Y., & Wang, B. (2020). Dominant process for northward propagation of boreal summer intraseasonal oscillation over the western North Pacific. *Geophysical Research Letters*, 47(22), e2020GL089808. <https://doi.org/10.1029/2020gl089808>
- Yang, Y. M., Wang, B., & Lee, J. Y. (2019). Mechanisms of northward propagation of boreal summer intraseasonal oscillation revealed by climate model experiments. *Geophysical Research Letters*, 46(6), 3417–3425. <https://doi.org/10.1029/2018gl081612>
- Yasunari, T. (1979). Cloudiness fluctuations associated with the Northern Hemisphere summer monsoon. *Journal of the Meteorological Society of Japan*, 57(3), 227–242. [https://doi.org/10.2151/jmsj1965.57.3\\_227](https://doi.org/10.2151/jmsj1965.57.3_227)
- Yasunari, T. (1980). A quasi-stationary appearance of 30–40 day period in the cloudiness fluctuations during the summer monsoon over India. *Journal of the Meteorological Society of Japan*, 58(3), 225–229. [https://doi.org/10.2151/jmsj1965.58.3\\_225](https://doi.org/10.2151/jmsj1965.58.3_225)
- Yihui, D., Chongyin, L., & Yanju, L. (2004). Overview of the South China sea monsoon experiment. *Advances in Atmospheric Sciences*, 21(3), 343–360. <https://doi.org/10.1007/BF02915563>
- Zhang, C. (2013). Madden-Julian Oscillation: Bridging weather and climate. *Bulletin of the American Meteorological Society*, 94(12), 1849–1870. <https://doi.org/10.1175/BAMS-D-12-00026.1>